Materials & Design 227 (2023) 111722

Contents lists available at ScienceDirect

Materials & Design

journal homepage: www.elsevier.com/locate/matdes

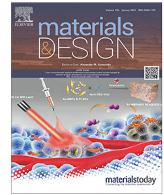

Superior oxidation resistance of the chemically complex but structurally simple Ti-Al-Ta-Ce-Si-La-B-nitride

P.H. Mayrhofer [a,*], S. Kagerer [a], P. Polcik [b], A. Kirnbauer [a]

[a] Institute of Materials Science and Technology, TU Wien, Vienna A-1060, Austria
[b] Plansee Composite Materials GmbH, D-86983 Lechbruck am See, Germany

HIGHLIGHTS

- Ta, $CeSi_2$, and LaB_6 show a cumulative effect on strength and stability for (Ti, Al)N.
- Slowest oxidation kinetic (k_p = 0.399 $\times$ 10^{-5} $\mu m^2/s$ @ 900 °C) for the $CeSi_2$ + LaB_6 alloyed (Ti,Al,Ta)N.
- $CeSi_2$ and LaB_6 allow to simultaneously use the benefits of Si, B, and the reactive element effect.
- $CeSi_2$ and LaB_6 are beneficial over their elemental form also for the target production.

GRAPHICAL ABSTRACT

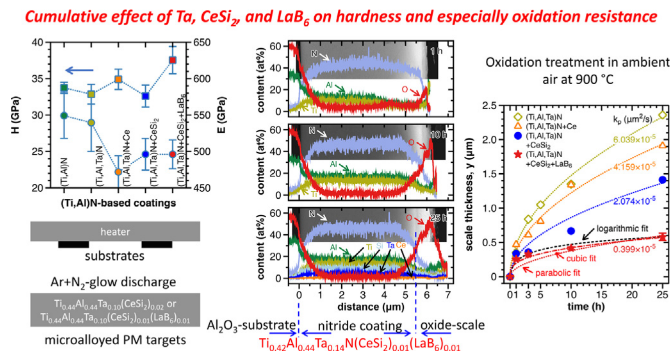

ARTICLE INFO

Article history:
Received 17 November 2022
Revised 1 February 2023
Accepted 9 February 2023
Available online 11 February 2023

Keywords:
Ti-Al-N
Chemically complex nitrides
Thermal stability
Oxidation resistance
Reactive element effect

ABSTRACT

Alloying (Ti,Al)N with Ta, $CeSi_2$ or LaB_6 is beneficial for both hardness and thermal stability. Here we show that their different mechanisms allow for a cumulative improvement when alloyed together, which is especially pronounced for the oxidation resistance. During isothermal oxidation treatments in ambient air at 900 °C (for up to 25 h), $Ti_{0.44}Al_{0.44}Ta_{0.12}N$ allows for a parabolic scale growth rate constant k_p of 6.039 $\times$ 10^{-5} $\mu m^2/s$. This is reduced to 2.074 $\times$ 10^{-5} and even 0.399 $\times$ 10^{-5} $\mu m^2/s$ when alloying with 2 mol% $CeSi_2$ respectively $CeSi_2$ + LaB_6 (1 mol% each). The oxide scale growth kinetics for the latter can be even better described by a logarithmic or cubic law. In the as-deposited state the $CeSi_2$ and $CeSi_2$ + LaB_6 alloyed (Ti,Al,Ta)N are single-phase fcc structured providing an indentation hardness of 32.6 ± 1.5 and 37.8 ± 1.5 GPa, combined with an indentation modulus of 496 ± 22 and 496 ± 14 GPa, respectively. After vacuum-annealing at 1000 °C, their hardness is still 33.0 ± 1.6 and 34.8 ± 1.1 GPa, and noticeable formation of hexagonal AlN and TaN_x phases can only be detected by X-ray diffraction when annealed at temperatures above 1200 °C.

Using $CeSi_2$ and LaB_6 instead of their elemental form is furthermore beneficial for the target production itself, as Ce and La are highly reactive.

© 2023 The Author(s). Published by Elsevier Ltd. This is an open access article under the CC BY-NC-ND license (http://creativecommons.org/licenses/by-nc-nd/4.0/).

1. Introduction

Face centered cubic (fcc) structured (Ti,Al)N-based hard coatings are most prominently used to protect machining tools and components especially against a severe combination of mechanical and thermal loading [1,2]. For machining operations, thereby pro-

* Corresponding author.
E-mail address: paul.mayrhofer@tuwien.ac.at (P.H. Mayrhofer).

https://doi.org/10.1016/j.matdes.2023.111722
0264-1275/© 2023 The Author(s). Published by Elsevier Ltd.
This is an open access article under the CC BY-NC-ND license (http://creativecommons.org/licenses/by-nc-nd/4.0/).

tected tools allow for increased cutting speeds, reduced coolant flows, and even dry machining [3]. A significant improvement of (Ti,Al)N coatings – besides their optimization via growth morphology and Al content [4] – has been achieved through alloying with additional elements [5], out of which Si and Ta are explicitly mentioned.

An optimized addition of Si (typically only up to a few at%) allows for a dense growth morphology, increased cohesive strength of grain and column boundaries, and increased mechanical strength and thermal stability with outstanding oxidation resistance [6–10]. "A lot helps a lot" has its limits as the Si content needs to be balanced to the Al content to avoid the formation of the hexagonal close packed wurtzite-type AlN-based phase (simply abbreviated here with w-AlN to indicate its structural difference from another important hexagonal phase in this work, h-Ta_2N, being Fe_2N-type [11,12]) as well as an excessive Si-N-based boundary phase – both of which typically reduce the mechanical strength [9,10,13,14]. An optimized addition of Si to TiN furthermore helped to increase its fracture toughness to 4.5 ± 0.6 MPa$\sqrt{m}$ [15].

The addition of Ta also allows for increased thermomechanical properties as well as oxidation resistance [16,17], and even increased fracture toughness values (up to 4.7 ± 0.2 MPa$\sqrt{m}$) are reported for (Ti,Al)N when alloyed with Ta [18]. Again, too much is counteractive and the maximum or optimized Ta content also depends on the Ti content – optimal Ta/Ti ratios for improved oxidation resistance of fcc-(Ti,Al,Ta)N coatings are reported to be ~1/3 [19]. Important to mention is that the available N-supply needs attention as well. This is valid for Si as well as Ta addition as both promote the formation of other stoichiometric nitrides than the 1:1 preferred by Ti and Al – this unfortunately is sometimes not taken care of.

However, the mechanisms of Si and Ta for improved oxidation resistance, mechanical strength, and fracture toughness are different. Increasing the mechanical strength via the addition of Si is rather straight forward as thereby a dense growth morphology is obtained and especially the cohesive strength of the typically weak grain and column boundaries is improved. Adding Ta not always improves the mechanical strength of (Ti,Al)N, even if the coatings seem to be single-phase fcc structured. The reasons might partly be in the energetically promoted formation of vacancies for TaN_x with respect to TiN or AlN, which strongly depends on the available N-supply and N_2 chemical potential. Lower N-supply and N_2 chemical potentials promote the formation of N-vacancies for fcc-TaN_x, even up to 50 % vacancies of the N-sublattice (i.e., $TaN_{0.5}$) [20]. Thus, not only the formation of hexagonal TaN_x phases need to be considered (when alloying Ta to (Ti,Al)N), but also the metal/non-metal ratio in an otherwise single-phase fcc-structured (Ti,Al)N.

The improved oxidation resistance of (Ti,Al)N through the alloying with Si is based on multiple effects like a retarded anatase-to-rutile TiO_2 phase transformation, a promoted outermost Al_2O_3 layer formation, and a dense and well-adherent Si-rich oxide formation at the oxide/nitride interface [9]. Tantalum on the other side, promotes the formation of a dense and well-adherent rutile-structured Ti-rich inner oxide-scale on (Ti,Al)N (with an outermost Al_2O_3-based scale), resulting in reduced oxide growth kinetics when compared with (Ti,Al)N [16–18].

Recently, we showed that already the small addition of 1–2 at% Ce (metal fraction) to (Ti,Al)N also leads to an increased hardness, thermal stability as well as oxidation resistance [21]. The latter is based on the Ce-promoted formation of a dense and well-adherent alumina-based oxide scale [21] – also known as the reactive element effect in chromia and alumina formers – and thus deviates from the mechanism provided by Ta. Small additions of reactive elements such as Ce and La to structural and coating materials – especially those on which chromia or alumina scales form – are beneficial for their oxidation protection, but they can also enhance their mechanical properties [22–30]. The combined alloying of (Ti,Al)N with Ce and Si further improves hardness, thermal stability, and oxidation resistance [31]. This had another positive impact, as for the powder metallurgical prepared target development the more oxidation resistant $CeSi_2$ powder could be used instead of the reactive element Ce. A corresponding improvement in hardness, thermal stability, and oxidation resistance of (Ti,Al)N is also reported through the alloying with LaB_6 (using an LaB_6 alloyed Ti-Al target) [32], although with a slight advantage for $CeSi_2$. These studies additionally show that the Ta, $CeSi_2$, and LaB_6 alloyed Ti-Al targets allow for an increased sputter rate compared with Ti-Al (improvements by a factor of up to 2.3 [21,31–33] are reported).

The synergistic effects of these elements (Ta and $CeSi_2$ as well as LaB_6), motivated us to study their combination. Therefore, we developed nitride coatings sputtered from $CeSi_2$ alloyed (2 mol%) as well as $CeSi_2$ plus LaB_6 alloyed (1 mol% each) Ti-Al-Ta targets. These two different coatings were studied with respect to their phase composition, crystal structure, mechanical properties (indentation hardness *H* and indentation modulus *E*), as well as thermal stability (vacuum annealing treatments up to 1300 °C) and oxidation resistance (ambient air exposure at 900 °C for up to 25 h). The results are presented and discussed in context with earlier studies [33] of correspondingly prepared (Ti,Al)N, (Ti,Al,Ta)N, and Ce alloyed (Ti,Al,Ta)N coatings.

2. Experimental

$CeSi_2$ alloyed and $CeSi_2$ + LaB_6 alloyed (Ti,Al,Ta)N coatings were developed by magnetically unbalanced magnetron sputtering of 3-inch $Ti_{0.44}Al_{0.44}Ta_{0.10}(CeSi_2)_{0.02}$ and $Ti_{0.44}Al_{0.44}Ta_{0.10}(CeSi_2)_{0.01}(LaB_6)_{0.01}$ compound targets, respectively, with a mixed Ar + N_2 glow discharge (both gases of 99.999 % purity). These powder metallurgical targets (purity of at least 99.7 %) are developed by Plansee Composite Materials GmbH via alloying 2 mol% $CeSi_2$ respectively 1 mol% $CeSi_2$ plus 1 mol% LaB_6 to the Ti-Al-Ta composite (with an Al/Ti ratio of 1 and to have 10 at% Ta in the final target composition) [34]. The deposition system is based on a Leybold Heraeus Z400, which features a shutter between the parallel facing target and substrate holder (the used substrate-to-target distance was 4 cm). Prior to loading the substrates [(1–102)-oriented sapphire (10 × 10 × 0.53 mm^3), polycrystalline Al_2O_3 (20 × 7 × 0.38 mm^3), austenitic steel platelets, as well as low-alloy steel foils] to the deposition chamber, they were cleaned in an ultrasonic acetone and ethanol bath for 5 min each.

After reaching a base pressure of at least 5 × 10^{-4} Pa, the substrates were heated to T_s = 430 ± 20 °C and Ar-ion etched at a pressure of 1.3 Pa (the Ar flow F_{Ar} was set to 120 sccm) for 10 min (with an Ar glow-discharge between substrate and shutter, through applying a pulsed DC substrate potential of −150 V, pulse frequency = 150 kHz, and pulse duration = 2496 ns). Also, the targets were pre-cleaned with this Ar pressure (powering the magnetron with a DC current of I_m = 1 A) for the last 3 min of the substrate etching process. After this, the parameters were adjusted for the deposition – T_s and I_m were not changed, the substrate bias potential was set to −50 V DC, F_{Ar} was reduced to 24 sccm and the N_2 flow F_{N2} was set to 8 sccm (resulting in an N_2-flow rate ratio f_{N2} = $F_{N2}/(F_{N2} + F_{Ar})$ of 0.25 and a total pressure of ~0.35 Pa) – and the shutter was removed to start the deposition for 20 min.

The chemical compositions of as-deposited coatings are obtained by energy dispersive X-ray spectroscopy (EDS). Their growth-morphology is studied via fracture cross sections by scanning electron microscopy (SEM, field emission gun FEGSEM Quanta

200). Structure and qualitative phase analysis of as-deposited as well as vacuum-annealed coatings are conducted by Bragg-Brentano X-ray diffraction (XRD) with monochromatic Cu K_α radiation (Empyrean PANalytical diffractometer). To avoid any substrate interference for these detailed XRD studies powdered free-standing coating material was used, which was obtained by chemically dissolving the coated Fe-foil with 10 % nitric acid at 40 °C. The thereby obtained free-standing coating fragments were ground to fine powder with a ceramic mortar.

Indentation hardness (*H*) and modulus (*E*) of the coatings (as-deposited and after vacuum annealing) on (1–102)-oriented sapphire are obtained through nanoindentation experiments using an UMIS II nanoindentation system equipped with a Berkovich tip, following the procedures described in Refs. [35–38] and assuming a film Poisson ratio of 0.25.

The as-deposited coatings [on (1–102)-oriented sapphire substrates and powdered free-standing coating material] are vacuum-annealed at temperatures *T* of 800, 900, 1000, 1100, 1200, and 1300 °C for 10 min (at *T*) using a Centorr LF22-2000 vacuum furnace (heating rate was 20 K/min and cooling rate by turning off the heater was > 50 K/min down to 100 °C). Additionally, the coatings on sapphire are oxidized in ambient air at 900 °C for 1, 3, 5, 10, and 25 h within a Nabertherm furnace, after which the oxide scale was investigated by SEM and EDS line-scans of the metallographically embedded and polished cross sections. The oxide scale thickness value is the mean of 5 measurements (with ~1 µm spacing between measurement points) on each of these samples during their SEM studies.

3. Results and discussion

3.1. Chemical composition, structure and growth morphology

The chemical compositions of the $CeSi_2$ and $CeSi_2$ + LaB_6 alloyed (Ti,Al,Ta)N coatings are summarized in Table 1, with respect to the target from which they were prepared. Their metal fractions are close to those of the respective target, with only slightly higher Ta contents. To account for the uncertainty of EDS especially for light elements, the $CeSi_2$ and LaB_6 fractions are based on the Ce and La content, respectively.

Additionally, the metal as well as $CeSi_2$ and LaB_6 content is related to the sum of Ti + Al + Ta, to indicate that it is still open how $CeSi_2$ and LaB_6 are distributed among the material (which element is at which sublattice or phase is unknown except for Ti, Al, and Ta).

Thus, their nomenclature would be $Ti_{0.43}Al_{0.43}Ta_{0.14}N(CeSi_2)_{0.02}$ and $Ti_{0.42}Al_{0.44}Ta_{0.14}N(CeSi_2)_{0.01}(LaB_6)_{0.01}$, but for easier reading these are also referred to as $CeSi_2$ and $CeSi_2$ + LaB_6 alloyed (Ti,Al,Ta)N. XRD studies of powdered free-standing coating materials (after chemical dissolution of their low-alloy steel substrates) clearly show their single-phase TiN-based fcc structure, corresponding to that of (Ti,Al)N, (Ti,Al,Ta)N, and (Ti,Al,Ta)N+Ce (from Ref. [33]), Fig. 1. The respective XRD peak positions indicate lattice parameters of 4.21 ± 0.01 Å for both coatings.

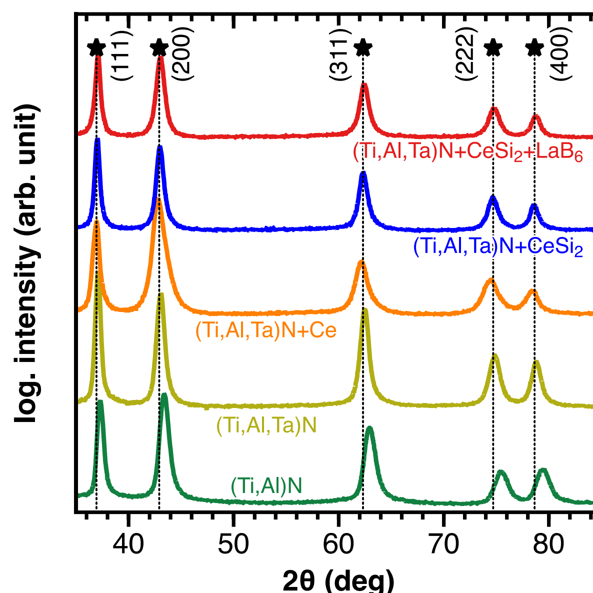

Fig. 1. X-ray diffraction patterns of $Ti_{0.43}Al_{0.57}N$, $Ti_{0.4}Al_{0.44}Ta_{0.12}N$, $Ti_{0.43}Al_{0.42}Ta_{0.14}Ce_{0.01}N$, $Ti_{0.43}Al_{0.43}Ta_{0.14}N(CeSi_2)_{0.02}$, and $Ti_{0.43}Al_{0.43}Ta_{0.14}N(CeSi_2)_{0.01}(LaB_6)_{0.01}$ coatings (removed from their substrate and grind to powders). The data for (Ti,Al)N, (Ti,Al,Ta)N, and (Ti,Al,Ta)N + Ce are from [33].

The growth rates (*R*) of $Ti_{0.43}Al_{0.43}Ta_{0.14}N(CeSi_2)_{0.02}$ and $Ti_{0.42}Al_{0.44}Ta_{0.14}N(CeSi_2)_{0.01}(LaB_6)_{0.01}$ are with 225 and 305 nm/min, respectively, much higher than that of $Ti_{0.43}Al_{0.57}N$ ($R \sim 77$ nm/m in [32]), which was prepared with the identical deposition conditions and system. For comparison, the $Ti_{0.44}Al_{0.44}Ta_{0.12}N$ and $Ti_{0.43}Al_{0.42}Ta_{0.14}Ce_{0.01}N$ coatings yield growth rates of 239 and 209 nm/min, respectively [33].

The increased deposition rate when using heavy-element alloyed Ti-Al targets can be attributed to a higher volume-density of collision cascades in the surface-near regions of the target and enhanced secondary electron emission, which is especially the case for the Ta + $CeSi_2$ + LaB_6 alloyed $Ti_{0.5}Al_{0.5}$ target. The latter allows for the highest *R* of 305 nm/min among these coatings investigated. However, contrary to $Ti_{0.44}Al_{0.44}Ta_{0.12}N$, which exhibits a clearly visible columnar growth throughout the entire coating thickness, Fig. 2a, the addition of Ce already causes the column size to decrease, Fig. 2b, which is even more pronounced for the $CeSi_2$ and $CeSi_2$ + LaB_6 alloyed (Ti,Al,Ta)N, Fig. 2c and d, respectively.

The latter even exhibits an almost featureless cross-section, which we attribute to the combined effects of the heavy elements Ce and La as well as the well-reported grain-refinement effects of Si and B. Please note that the N_2-partial pressure for sputtering the individually alloyed Ti-Al targets was unchanged, although the deposition rates hugely increase with alloying content.

Table 1
EDS results of our $CeSi_2$-alloyed and $CeSi_2$–LaB_6-alloyed Ti–Al–Ta–N coatings with respect to the respective target composition (the total pressure was 0.35 Pa, the N_2-to-total-pressure ratio was 0.2, the target current was 1.0 A, the substrate temperature was 430 ± 20 °C). X refers to either Ti, Al, Ta, $CeSi_2$, or LaB_6.

Target composition (mol%)					Film composition (at%)								X/(Ti + Al + Ta) (-)				
Ti	Al	Ta	$CeSi_2$	LaB_6	Ti	Al	Ta	Ce	Si	La	B	N	Ti	Al	Ta	$CeSi_2$	LaB_6
44.0	44.0	10.0	2.0	–	18.2	18.3	6.0	0.7	2.1	–	–	54.7	0.43	0.43	0.14	0.02	–
44.0	44.0	10.0	1.0	1.0	15.6	16.4	5.0	0.4	1.9	0.5	4.3	55.9	0.42	0.44	0.14	0.01	0.01

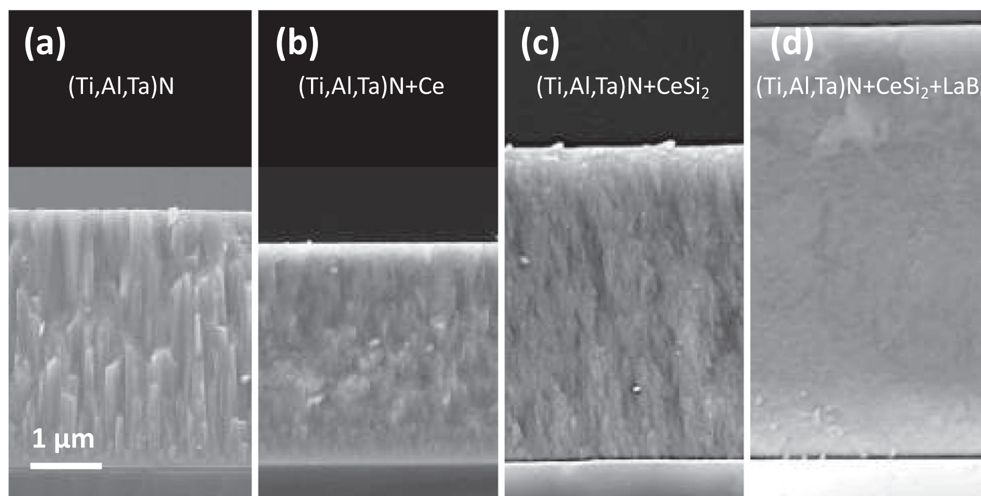

Fig. 2. Fracture cross-sectional SEM micrographs of as-deposited **(a)** $Ti_{0.44}Al_{0.44}Ta_{0.12}N$, **(b)** $Ti_{0.43}Al_{0.42}Ta_{0.14}Ce_{0.01}N$, **(c)** $Ti_{0.43}Al_{0.43}Ta_{0.14}N(CeSi_2)_{0.02}$, and **(d)** $Ti_{0.43}Al_{0.43}Ta_{0.14}N(CeSi_2)_{0.01}(LaB_6)_{0.01}$ coatings on Si substrates. The scale bar marks also the interface between nitride coating and substrate (please note that the deposition time for **(a)** $Ti_{0.44}Al_{0.44}Ta_{012}N$ and **(b)** $Ti_{0.43}Al_{0.42}Ta_{0.14}Ce_{0.01}N$ was 15 min [33], while for **(c)** $Ti_{0.43}Al_{0.43}Ta_{0.14}N(CeSi_2)_{0.02}$ and **(d)** $Ti_{0.43}Al_{0.43}Ta_{0.14}N(CeSi_2)_{0.01}(LaB_6)_{0.01}$ it was 20 min).

3.2. Mechanical properties

The hardness, *H*, of the ($CeSi_2$) alloyed (Ti,Al,Ta)N is with 32.6 ± 1.5 GPa very similar to that of $Ti_{0.43}Al_{0.57}N$, $Ti_{0.44}Al_{0.44}Ta_{0.12}N$, and $Ti_{0.43}Al_{0.42}Ta_{0.14}Ce_{0.01}N$ having 33.7 ± 0.7, 32.9 ± 1.4, and 34.9 ± 1.4 GPa, respectively, see Fig. 3.

However, when using LaB_6 as an additional ingrediency to $CeSi_2$, to obtain the $CeSi_2$ + LaB_6 alloyed (Ti,Al,Ta)N, the hardness increases to 37.8 ± 1.5 GPa. This coating exhibits the finest growth morphology among the four (Ti,Al,Ta)N coatings compared here (Fig. 2). Hence, grain refinement strengthening (as described by the Hall–Petch relationship [39–41]) is most pronounced here. However, as $Ti_{0.43}Al_{0.42}Ta_{0.14}Ce_{0.01}N$ exhibits also a much finer growth morphology than $Ti_{0.44}Al_{0.44}Ta_{0.12}N$, but their hardness values are comparable, the data indicate that Si and B additionally improve bond strength and cohesive strength of the grain and column boundaries [6–8]. The even slightly decreased hardness for the $CeSi_2$ alloyed (Ti,Al,Ta)N with respect to the Si-free and only Ce alloyed one, might be a consequence of the not adapted N_2-partial pressure. The $Ti_{0.44}Al_{0.44}Ta_{0.10}(CeSi_2)_{0.02}$ target allows for an even higher sputter rate than the $Ti_{0.44}Al_{0.44}Ta_{0.10}Ce_{0.02}$ target, delivering more metallic species to the growing film. Thus, the metal-to-nitrogen arrival ratio (for the same N_2-partial pressure) is higher for the $CeSi_2$ alloyed (Ti,Al,Ta)N than for the Ce-alloyed one.

The 2 mol% $CeSi_2$ alloyed (Ti,Al)N coating (Ta-free) does provide an ~4 GPa higher hardness than its Si-free relative ($Ti_{0.48}Al_{0.50}Ce_{0.02}N$) [31]. Similarly, the 1 mol% LaB_6 alloyed (Ti,Al)N coating (Ta-free) is with 39.3 ± 2.1 GPa much harder than $Ti_{0.43}Al_{0.57}N$ [32], Fig. 3a. These data – which are all obtained with the same deposition conditions, equipment, and N_2-partial pressure – suggest that especially with the presence of Ta, the N_2-partial pressure needs attention with respect to the provided metal flux.

While the hardness is highest for the $CeSi_2$ + LaB_6 alloyed (Ti,Al,Ta)N among the four (Ti,Al,Ta)N coatings, its indentation modulus, *E*, is among the lowest with 496 ± 14 GPa. The $CeSi_2$ alloyed one provides a similar value of 496 ± 22 GPa. Consequently, the H/E (elastic strain to failure) and H^3/E^2 (resistance to plastic deformation) ratios are highest for $Ti_{0.42}Al_{0.44}Ta_{0.14}N(CeSi_2)_{0.01}(LaB_6)_{0.01}$, suggesting for a higher wear resistance and in particular toughness [42,43].

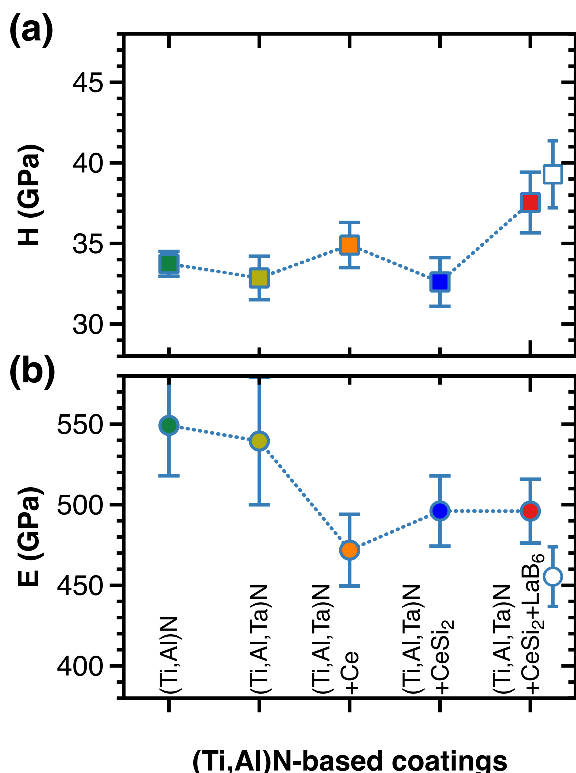

Fig. 3. **(a)** Indentation hardness, *H*, and **(b)** indentation modulus, *E*, of as-deposited $Ti_{0.43}Al_{0.57}N$, $Ti_{0.44}Al_{0.44}Ta_{0.12}N$, $Ti_{0.43}Al_{0.42}Ta_{0.14}Ce_{0.01}N$, $Ti_{0.43}Al_{0.43}Ta_{0.14}N(CeSi_2)_{0.02}$, and $Ti_{0.43}Al_{0.43}Ta_{0.14}N(CeSi_2)_{0.01}(LaB_6)_{0.01}$ coatings on sapphire substrates. The data for (Ti,Al)N, (Ti,Al,Ta)N, and (Ti,Al,Ta)N + Ce are from [33]. The single data point (empty symbol) in **(a)** and **(b)** is for the Ta-free 2 mol% LaB_6-alloyed $Ti_{0.43}Al_{0.57}N$ [32].

3.3. Thermal stability

Corresponding to the previous studies on (Ti,Al,Ta)N and Ce alloyed (Ti,Al,Ta)N (i.e., $Ti_{0.44}Al_{0.44}Ta_{0.12}N$ and $Ti_{0.43}Al_{0.42}Ta_{0.14}Ce_{0.01}N$), the thermal stability of the $CeSi_2$ and $CeSi_2$ + LaB_6 alloyed (Ti,Al,Ta)N was studied via vacuum annealing of powdered coating material and subsequent XRD measurements, see Fig. 4. We use the previously investigated $Ti_{0.44}Al_{0.44}Ta_{0.12}N$ as a reference [33], which maintains an fcc solid solution up to an annealing tempera-

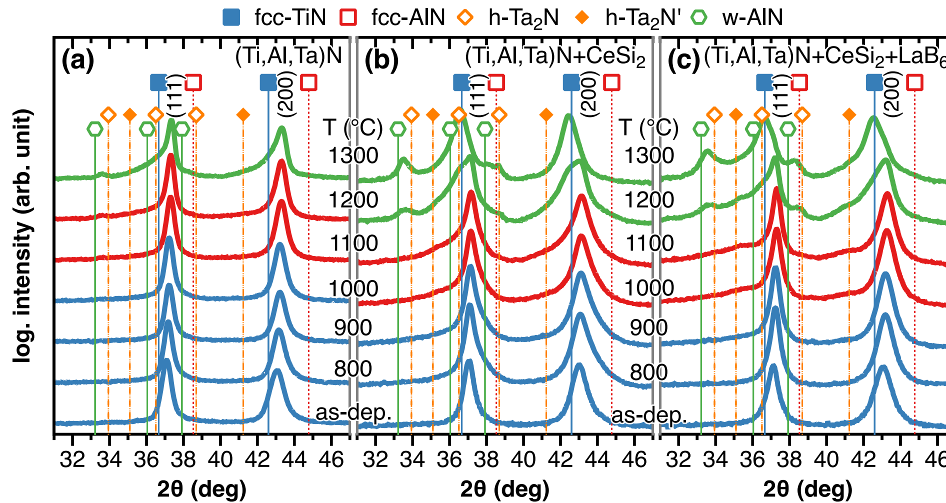

Fig. 4. XRD patterns from the powders of **(a)** $Ti_{0.44}Al_{0.44}Ta_{0.12}N$, **(b)** $Ti_{0.43}Al_{0.43}Ta_{0.14}N(CeSi_2)_{0.02}$, and **(c)** $Ti_{0.43}Al_{0.43}Ta_{0.14}N(CeSi_2)_{0.01}(LaB_6)_{0.01}$ coatings, in their as-deposited state and after vacuum-annealing for 10 min at T = 800, 900, 1000, 1100, 1200, and 1300 °C (from bottom to top). The data for (Ti,Al,Ta)N are from [33]. Peak positions of ICDD reference data are indicated: blue squares fcc-TiN (#00–038-1420), red empty squares fcc-AlN (#00–046-1200), empty green hexagons w-AlN (#00–025-1133), orange empty diamond h-Ta_2N (#00–026-0985). The orange diamonds indicate the positions for an ordered structure of the latter, h-Ta_2N', as suggested by [44]. (For interpretation of the references to colour in this figure legend, the reader is referred to the web version of this article.)

ture of T = 1000 °C. For higher temperatures, the evolving small XRD peak at ~33.8° indicates the formation of the hexagonal wurtzite-type AlN (w-AlN), which is characteristic for (Ti,Al)N-based coatings and typically follows a spinodal decomposition. The small peak at ~41.5°, which is present for T = 1300 °C as a left-hand shoulder of the 200-peak, indicates the formation of the hexagonal structured Ta_2N. Actually, as suggested by [44], only the ordered form of h-Ta_2N exhibits this superstructure reflex. The corresponding reflexes at 35.1° and 41.2° are therefore indexed with h-Ta_2N' in Fig. 4. Already at 1200 °C the slightly increased background-level at this diffraction angle might be due to this Ta_2N formation.

The $CeSi_2$ and $CeSi_2$ + LaB_6 alloyed (Ti,Al,Ta)N do show corresponding changes of their XRD response already after annealing at 1000 °C, with the tendency of slightly more pronounced small XRD peak formation at ~35.5 and 41.5° (and thus hexagonal phase formation) for the $CeSi_2$ + LaB_6 alloyed (Ti,Al,Ta)N. Especially the earlier onset of the h-Ta_2N formation might be a consequence of the not optimized N_2-partial pressure during their deposition. For example, $Ti_{0.43}Al_{0.42}Ta_{0.14}Ce_{0.01}N$ as well as the 2 mol% $CeSi_2$ alloyed (Ti,Al)N exhibit signs for an hexagonal phase formation only after annealing at 1200 °C [31,33].

These structural changes are essentially responsible for the coating's response to nanoindentation when annealed at T, Fig. 5. The $CeSi_2$ + LaB_6 alloyed (Ti,Al,Ta)N – although starting at a higher value – shows a slightly earlier decline in H with increasing T above 900 °C than the $CeSi_2$ alloyed (Ti,Al,Ta)N. However, after annealing at 1000 °C, the $CeSi_2$ alloyed and the $CeSi_2$ + LaB_6 alloyed (Ti,Al,Ta)N coatings still yield 33.0 ± 1.6 and 34.8 ± 1.1 GPa, respectively, Fig. 5a. During annealing at 1100 °C, both coatings experienced crack formation and spallation. This coincides with the annealing temperature at which more pronounced XRD peaks at the positions for w-AlN and h-Ta_2N phases are present.

Contrary, the (Ti,Al,Ta)N coating [33] allowed annealing at 1100 °C, after which it exhibits a higher hardness (35.5 ± 1.5 GPa) than in the as-deposited state (32.9 ± 1.3 GPa), stemming from age-hardening processes. Nanoindentation shows that this already sets in for T = 900 °C, Fig. 5, although XRD indicates nearly no change up to T = 1000 °C. But as nicely shown by Rachbauer et al. [45] – actually for the same annealing temperature of 900 °C – even if XRD suggests for no significant changes (except

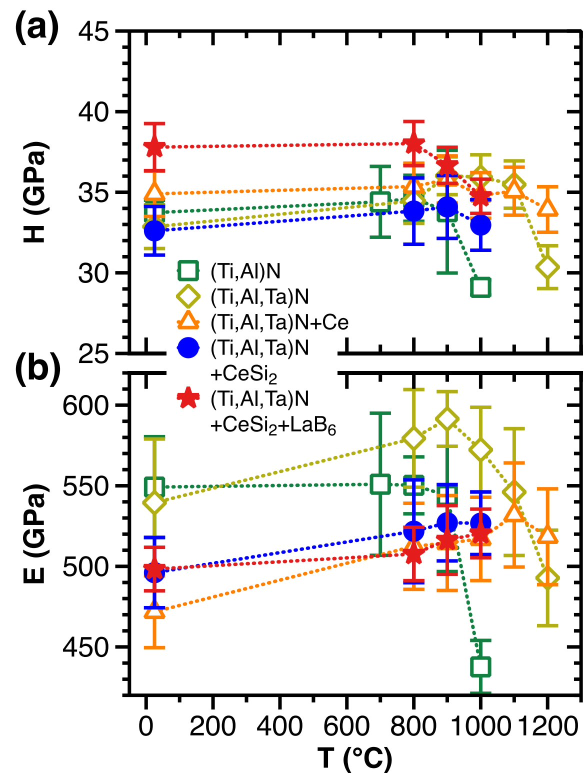

Fig. 5. **(a)** Indentation hardness, H, and **(b)** indentation modulus, E of $Ti_{0.43}Al_{0.57}N$, $Ti_{0.44}Al_{0.44}Ta_{0.12}N$, $Ti_{0.43}Al_{0.42}Ta_{0.14}Ce_{0.01}N$, $Ti_{0.43}Al_{0.43}Ta_{0.14}N(CeSi_2)_{0.02}$, and $Ti_{0.43}Al_{0.43}Ta_{0.14}N(CeSi_2)_{0.01}(LaB_6)_{0.01}$ coatings on sapphire substrates in their as-deposited state and after vacuum-annealing at T = 800, 900, 1000, 1100, and 1200 °C. The error bars represent the standard deviations from the mean values obtained from up to 20 film-only H and E values for each sample. The data for (Ti,Al)N, (Ti,Al,Ta)N, and (Ti,Al,Ta)N + Ce (empty symbols) are from [33].

for a small shift in XRD peak positions, as also obtained here) atom probe tomography yields ongoing spinodal decomposition. This also caused the hardness of (Ti,Al)N to increase when annealed at 900 °C, like for the (Ti,Al,Ta)N coating presented here. Annealing at 1200 °C, at which for (Ti,Al,Ta)N now also more pronounced

peaks at the positions of w-AlN and h-Ta_2N are present, causes the hardness to decrease to 30.4 ± 1.3 GPa.

For comparison we also added the data of the Ce alloyed (Ti,Al,Ta)N to Fig. 5, exhibiting a very similar trend as the $CeSi_2$ alloyed one, only that for this coating no crack formation or spallation occurred even during annealing at 1200 °C, after which the hardness was still 33.9 ± 1.4 GPa [33].

The two chemically complex coatings, the $CeSi_2$ and the $CeSi_2$ + LaB_6 alloyed (Ti,Al,Ta)N, exhibit together with the previously investigated Ce alloyed (Ti,Al,Ta)N the lower bound of the indentation moduli. Overall, the variation of E with T is similar to that of H; initially E increases with T until the formation of w-AlN and/or h-Ta_2N is significant. However, the variation in E seems to be more pronounced, please notice that the E axis covers a range of 200 GPa, while the H axis covers a range of 20 GPa, Fig. 5b.

The $CeSi_2$ and the $CeSi_2$ + LaB_6 alloyed (Ti,Al,Ta)N exhibited massive crack formation and spallation (from the sapphire substrate) when annealed at 1100 and 1200 °C. However interestingly, their indentation modulus continuously increases from ~496 to 525 GPa with increasing T to 1000 °C, contrary to their hardness, which tends to decrease for $T \geq 900$ °C.

Also the Ce alloyed (Ti,Al,Ta)N shows such a behavior. An explanation for this could be the variation in vacancy content [46,47]. We envision that with increasing chemical complexity the vacancy content increases as well and sputtering is generally known to favor such. Thus, in the as-deposited state these chemically most complex coatings might also contain a higher density of vacancies than (Ti,Al)N or (Ti,Al,Ta)N.

These additional vacancies are responsible for an increased hardness (upon vacancy hardening: the hardness increases as more obstacles for dislocation glide and sites for their pinning are present) but simultaneously decreased indentation modulus (as there are fewer metal–nitrogen bonds), with respect to (Ti,Al)N or (Ti,Al,Ta)N. Such a contradicting dependence of H and E on the vacancy content of nitrides was extremely nicely investigated and presented by Shin et al. [48] with the help of single-crystal TiN_x(001) layers.

Upon annealing the (Ti,Al,Ta)N-based materials, their vacancy content decreases to reach thermal equilibrium – in addition to other recovery processes where deposition-induced structural defects rearrange towards lower energy-sites. This ultimately causes the E modulus to increase but H to decrease as long as there is no change in crystal structure and overall distribution of elements.

The latter is mentioned because spinodal decomposition of e.g., fcc-(Ti,Al)N into Al-rich and Ti-rich fcc-(Ti,Al)N domains would cause E as well as H to increase [45], similar to strain hardening. Consequently, superposition of these processes (reduction in vacancy content and spinodal decomposition) can lead to a more pronounced increase in E than for H, or for a nearly constant H, as the overall impression of Fig. 5 suggests.

3.4. Oxidation resistance

In addition to the thermal stability investigations in vacuum, the oxidation resistance of the $CeSi_2$ and the $CeSi_2$ + LaB_6 alloyed (Ti,Al,Ta)N was investigated by exposing them to ambient air at 900 °C for 1, 3, 5, 10, and 25 h. To obtain the oxide scale thickness, the samples were embedded for their metallographic preparation, polished, and subsequently investigated using SEM and EDS. The oxide scale of the $CeSi_2$ alloyed (Ti,Al,Ta)N after 10 h at 900 °C is ~800 nm, Fig. 6a. For the most complex coating (additionally containing LaB_6) the oxide scale is even thinner, only ~450 nm, Fig. 6b. Still after 25 h the oxide scale is only ~550 nm, Fig. 6c.

To investigate in detail the depth of oxygen diffusion into the coating, EDS line-scans were taken on the $CeSi_2$ + LaB_6 alloyed

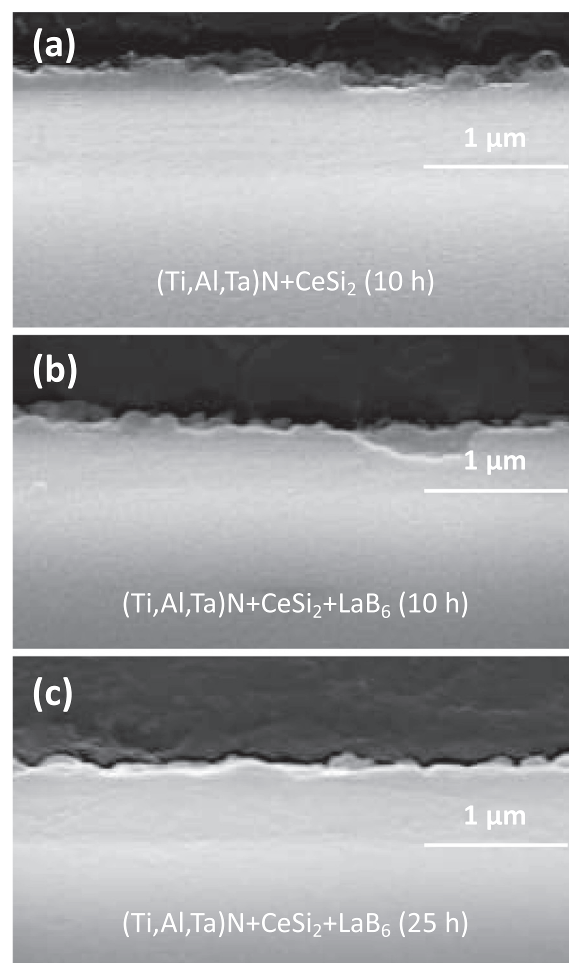

Fig. 6. Polished cross-sectional SEM images after oxidation at 900 °C for **(a)** $Ti_{0.43}Al_{0.43}Ta_{0.14}N(CeSi_2)_{0.02}$ after 10 h, **(b)** and **(c)** $Ti_{0.43}Al_{0.43}Ta_{0.14}N(CeSi_2)_{0.01}(LaB_6)_{0.01}$ after 10 and 25 h, respectively. The scale bar marks also the interface between nitride coating and oxide scale.

(Ti,Al,Ta)N coating after ambient-air-treatment at 900 °C for 1, 10, and 25 h, Fig. 7. The ~6-µm-thick coating shows only a tiny indication for an increased oxygen content at its surface-near region after 1 h, Fig. 7a. Increasing the oxidation time to 10 h causes this region to thicken to a few 100 nm. While the outermost region of the oxide is enriched in Al, the typically observed alternating Ti-rich and Al-rich layered oxide scale for (Ti,Al)N [49,50] is absent, Fig. 7b.

After 25 h, the oxygen-enriched outermost region thickened to ~0.7 µm; using the cross-over between N and O signal as the nitride coating/oxide scale interface and the afterwards rapid decline in O signal as the oxide scale surface (as shown by the corresponding SEM cross section added to Fig. 7c). This is in good agreement with SEM investigations, Fig. 6b and c, indicating ~450 and 550 nm thin oxide scales, respectively. EDS line-scans additionally reveal that the metals are homogenously distributed in the oxide scale, with a slightly enriched Al content within the outermost region.

When plotting the squared oxide scale thickness, y^2, over the oxidation time (1, 3, 10, 25 h), Fig. 8a, a linear dependence points to a parabolic oxide growth kinetic, with the slope representative for the parabolic rate constant k_p, according to [51,52]:

$$y^2 = k_p \cdot t + A_p \quad (1)$$

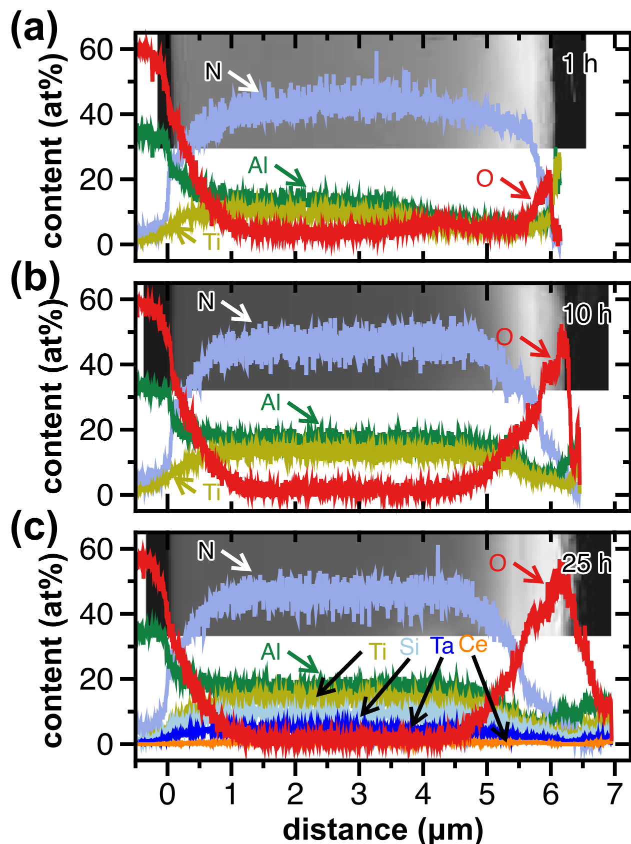

Fig. 7. EDS line-scans of $Ti_{0.43}Al_{0.43}Ta_{0.14}N(CeSi_2)_{0.01}(LaB_6)_{0.01}$ after oxidation at 900 °C for **(a)** 1 h, **(b)** 10 h, and **(c)** 25 h. For clarity, only in **(c)** the signals for Ce, Ta, and Si are added (similar profiles for La and B as for Ce and Si, respectively). Given is the distance from the nitride coating/sapphire substrate interface. The broad slopes of EDS lines are due to the relatively large spot size and depth of interaction of the EDS with not perfectly aligned interfaces.

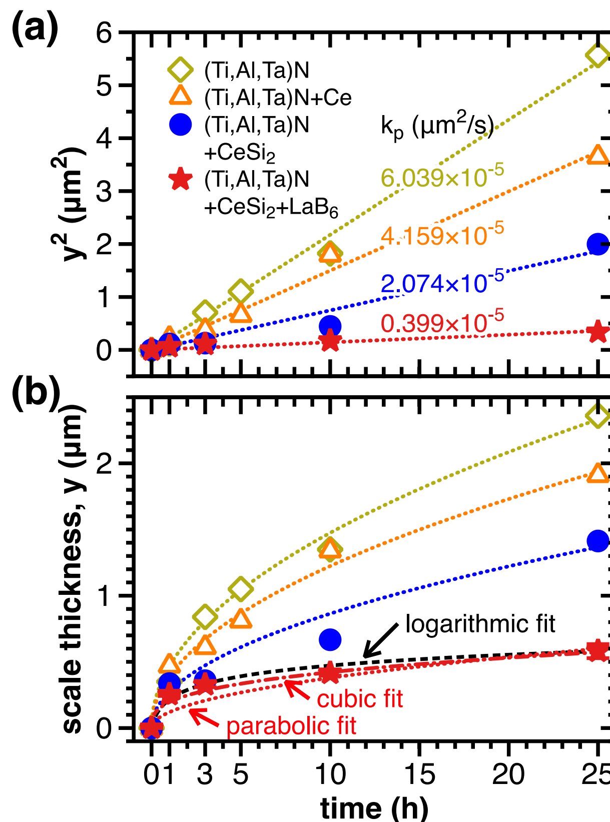

Fig. 8. **(a)** Squared and **(b)** linear oxide scale thickness, *y*, as a function of the oxidation time at 900 °C for $Ti_{0.44}Al_{0.44}Ta_{0.12}N$, $Ti_{0.43}Al_{0.42}Ta_{0.14}Ce_{0.01}N$, $Ti_{0.43}Al_{0.43}Ta_{0.14}N(CeSi_2)_{0.02}$, and $Ti_{0.43}Al_{0.43}Ta_{0.14}N(CeSi_2)_{0.01}(LaB_6)_{0.01}$ coatings on sapphire substrates. The slopes of the linear fits in **(a)** are used to draw the parabolic fits (dotted lines) for **(b)**. The latter show that the oxide growth kinetic of $Ti_{0.43}Al_{0.43}Ta_{0.14}N(CeSi_2)_{0.01}(LaB_6)_{0.01}$ is better described with a logarithmic law (dashed line) according to Eq (2) respectively a cubic law (dash-dotted line) according to Eq (3). The data for (Ti,Al)N, (Ti,Al,Ta)N, and (Ti,Al,Ta)N + Ce (empty symbols) are from [33]. The error bar is smaller than the symbol size.

with *t* for time and A_p for the corresponding constant. The $CeSi_2$ alloyed but especially the $CeSi_2$ + LaB_6 alloyed (Ti,Al,Ta)N yield the smallest slopes with k_p = 2.074 × 10^{-5} and 0.399 × 10^{-5} µm²/s, respectively, Fig. 8a.

These parabolic growth rates are significantly lower than the best ones ($Ti_{0.44}Al_{0.44}Ta_{0.12}N$ and $Ti_{0.43}Al_{0.42}Ta_{0.14}Ce_{0.01}N$) from a previous study comparing (Ti,Al)N, (Ti,Al,Ce)N, (Ti,Al,Ta)N, and (Ti,Al,Ta,Ce)N [33]. Compared with $Ti_{0.44}Al_{0.44}Ta_{0.12}N$ (k_p = 6.039 × 10^{-5} µm²/s), the $CeSi_2$ alloyed (Ti,Al,Ta)N offers a 3-times-lower k_p value, and the $CeSi_2$ + LaB_6 alloyed one an even 15-times-lower parabolic rate constant. In fact, Fig. 8b – plotting the oxide scale thickness linearly – shows that contrary to the other ones, the oxidation kinetics of $CeSi_2$ + LaB_6 alloyed (Ti,Al,Ta)N follows more a logarithmic law, with [51,52]:

$$y = k_{lg} \cdot \log\left(A_{lg} \cdot t + B\right) \quad (2)$$

or a cubic law:

$$y^3 = k_c \cdot t + A_c \quad (3)$$

The corresponding logarithmic rate constant k_{lg} is 0.12 µm, with the further constants of A_{lg} = 5 1/h and *B* = 1, and the corresponding cubic rate constant k_c is 0.205 × 10^{-5} µm³/s with A_c = 0 µm³.

On the basis of Wagner's oxidation theory [53], which considers ion diffusion through the oxide as the rate-determining step, Tammann [51] was the first to show experimentally that the growth kinetic of an oxide scale can be described with a parabolic law. This holds true if the oxide scale is dense, homogeneous, charge neutral, or relatively thick to achieve chemical equilibrium at the gas/oxide and oxide/metal interfaces, because then there is constant chemical potential gradient between these interfaces (hence, Fick's first law [54] applies). When the oxidation product deviates from these conditions, the kinetics also deviate from the parabolic law [55].

For thin oxide scales (thinner than the Debye length), the growth rate usually follows a logarithmic law according to the theory of Cabrera and Mott [56]. According to this, an electric field – resulting from the tunneling of electrons from the metal to chemically adsorbed oxygen species at the oxide surface – accelerates ion transport through the film, and the rate-determining step is the introduction of point defects into the oxide at the gas/oxide or oxide/metal interface. This behavior is often dominating at lower temperatures, so oxide growth at lower temperatures tends to follow the logarithmic law (if this is the case). The decrease in electric field with increasing film thickness results in a negligible growth rate once a limiting thickness is reached. The Debye length for Cr_2O_3 or Al_2O_3 with their inherently low defect concentration is a few 10 nm, so that space charges are present up to oxide scale thicknesses of a few 100 nm [55]. The model can be extended to thicker films if electron transport is possible via thermionic emission or via semiconducting oxides. This could contribute to the observation that the oxidation kinetics of the Si-containing high-entropy metal-sublattice nitride films (Al,Cr,Nb,Si,Ta,Ti)N [10] and (Al,Cr,Nb,Si,Ti)N [57], can be described by the logarithmic law even at 900 °C.

Sub-parabolic oxide scale growth (e.g., such as the cubic used here) is often associated with grain boundary mechanisms. For

example, the sub-parabolic oxidation kinetics of alumina scale on Fe–Cr–Al alloys (containing reactive elements) was explained by the fact that oxygen diffusion at oxide grain boundaries is the rate-determining step. In combination with oxide grain size increasing in the growth direction or with time, which causes a decrease in grain boundary density, this leads to a sub-parabolic scale growth (often close to cubic growth rates) [58].

4. Summary and conclusions

$CeSi_2$ and $CeSi_2$ + LaB_6 alloyed (Ti,Al,Ta) targets (specifically, powder metallurgically prepared $Ti_{0.44}Al_{0.44}Ta_{0.10}(CeSi_2)_{0.02}$ and $Ti_{0.44}Al_{0.44}Ta_{0.10}(CeSi_2)_{0.01}(LaB_6)_{0.01}$) allow for deposition rates of corresponding nitrides with 225 and 305 nm/min, respectively. These are in the range or even higher than the 239 nm/min for $Ti_{0.44}Al_{0.44}Ta_{0.12}N$ when sputtering a $Ti_{0.46}Al_{0.46}Ta_{0.08}$ target with the same N_2-partial pressure and power density. Both coatings crystallize single-phased with an fcc structure having a lattice parameter of 4.21 ± 0.01 Å. After vacuum annealing at 1000 °C, the hardness of the $CeSi_2$ alloyed (Ti,Al,Ta)N is 33.0 ± 1.6 GPa and thus even slightly above the 32.6 ± 1.5 GPa from its as-deposited state. The $CeSi_2$ + LaB_6 alloyed (Ti,Al,Ta)N is even harder with 37.8 ± 1.5 GPa (as-deposited), allowing for 34.8 ± 1.1 GPa when annealed at 1000 °C. During these annealing treatments their indentation moduli continuously increase from ~496 to 525 GPa. Only when annealed at higher temperatures, XRD indicates the formation of w-AlN and h-Ta_2N phases, but even at 1300 °C (highest temperature tested) the decomposition towards the individual stable constituents is not completed. However, more impressive is the oxidation resistance, which – when using a parabolic fit for the oxide scale thickness increase with time at 900 °C – yields parabolic growth rates k_p of 2.074×10^{-5} and 0.399×10^{-5} $\mu m^2/s$ for the $CeSi_2$ and $CeSi_2$ + LaB_6 alloyed (Ti,Al,Ta)N, respectively. The latter even allows for a 15-times lower growth rate than obtained for $Ti_{0.44}Al_{0.44}Ta_{0.12}N$ ($k_p = 6.039 \times 10^{-5}$ $\mu m^2/s$). In fact, while the oxide scale growth on (Ti,Al,Ta)N, Ce alloyed (Ti,Al,Ta) N, and $CeSi_2$ alloyed (Ti,Al,Ta)N nicely follow a parabolic rate, that on $CeSi_2$ + LaB_6 alloyed (Ti,Al,Ta)N can better be described with a logarithmic or cubic rate.

Based on our results we can conclude, that the small additions of $CeSi_2$ (2 mol%) and especially the combined addition of $CeSi_2$ +-LaB_6 (1 mol% each) to (Ti,Al,Ta)N is extremely beneficial for the growth morphology, mechanical strength, thermal stability, but especially the oxidation resistance.

Data availability

Data will be made available on request.

Declaration of Competing Interest

The authors declare that they have no known competing financial interests or personal relationships that could have appeared to influence the work reported in this paper.

Acknowledgment

PHM is supported by the Austrian COMET Program (project K2 InTribology1, no. 872176). The authors acknowledge the use of the facilities of USTEM and XRC at TU Wien (Austria), as well as TU Wien Bibliothek for financial support through its Open Access Funding Program.

Data Availability

The raw/processed data required to reproduce these findings can be made available upon request.

References

[1] W. Münz, Titanium aluminum nitride films: a new alternative to TiN coatings, J. Vac. Sci. Technol. A 4 (1986) 2717–2725, https://doi.org/10.1116/1.573713.
[2] O. Knotek, M. Böhmer, T. Leyendecker, On structure and properties of sputtered Ti and Al based hard compound films, J. Vac. Sci. Technol. A. 4 (1986) 2695–2700, https://doi.org/10.1116/1.573708.
[3] L. Chen, Y. Du, P.H. Mayrhofer, S.Q. Wang, J. Li, The influence of age-hardening on turning and milling performance of Ti-Al-N coated inserts, Surf. Coat. Technol. 202 (2008) 5158–5161, https://doi.org/10.1016/j.surfcoat.2008.05.036.
[4] C. Wüstefeld, D. Rafaja, V. Klemm, C. Michotte, M. Kathrein, Effect of the aluminium content and the bias voltage on the microstructure formation in Ti1−xAlxN protective coatings grown by cathodic arc evaporation, Surf. Coat. Technol. 205 (2010) 1345–1349, https://doi.org/10.1016/j.surfcoat.2010.07.057.
[5] D. Holec, L. Zhou, R. Rachbauer, P.H. Mayrhofer, Alloying-related trends from first principles: An application to the Ti-Al-X-N system, J. Appl. Phys. 113 (2013), https://doi.org/10.1063/1.4795590.
[6] S. Veprek, M. Jilek, Super- and ultrahard nanacomposite coatings: generic concept for their preparation, properties and industrial applications, Vacuum 67 (2002) 443–449, https://doi.org/10.1016/S0042-207X(02)00229-4.
[7] A. Flink, J.M. Andersson, B. Alling, R. Daniel, J. Sjölén, L. Karlsson, L. Hultman, Structure and thermal stability of arc evaporated (Ti0.33Al0.67)1−xSixN thin films, Thin Solid Films 517 (2008) 714–721, https://doi.org/10.1016/j.tsf.2008.08.126.
[8] S. Veprek, M.J.G. Veprek-Heijman, Industrial applications of superhard nanocomposite coatings, Surf. Coat. Technol. 202 (2008) 5063–5073, https://doi.org/10.1016/j.surfcoat.2008.05.038.
[9] Z.R. Liu, F. Pei, L. Chen, P.H. Mayrhofer, Effect of Si-addition on structure and thermal stability of Ti-Al-N coatings, J. Alloys Compd. 917 (2022) 165483 1–10, https://doi.org/10.1016/j.jallcom.2022.165483.
[10] A. Kretschmer, A. Kirnbauer, V. Moraes, D. Primetzhofer, K. Yalamanchili, H. Rudigier, P.H. Mayrhofer, Improving phase stability, hardness, and oxidation resistance of reactively magnetron sputtered (Al,Cr,Nb,Ta,Ti)N thin films by Si-alloying, Surf. Coat. Tech-nol. 416 (2021) 127162 1–12, https://doi.org/10.1016/j.surfcoat.2021.127162.
[11] T. Chihi, J.C. Parlebas, M. Guemmaz, First principles study of structural, elastic, electronic and optical properties of Nb_2N and Ta_2N compounds, Phys. Status Solidi B 248 (2011) 2787–2792, https://doi.org/10.1002/pssb.201147033.
[12] N. Schönberg, An X-ray study of the tantalum-nitrogen system, Acta Chem. Scand. 8 (1954) 199–203, https://doi.org/10.3891/acta.chem.scand.08-0199.
[13] W. Tillmann, M. Dildrop, Influence of Si content on mechanical and tribological properties of TiAlSiN PVD coatings at elevated temperatures surf, Coat. Technol. 321 (2017) 448–454, https://doi.org/10.1016/j.surfcoat.2017.05.014.
[14] S. Carvalho, L. Rebouta, A. Cavaleiro, L.A. Rocha, J. Gomes, E. Alves, Microstructure and mechanical properties of nanocomposite (Ti, Si, Al)N coatings, Thin Solid Films 398 (2001) 391–396, https://doi.org/10.1016/S0040-6090(01)01348-7.
[15] M. Sperr, Z.L. Zhang, Y.P. Ivanov, P.H. Mayrhofer, M. Bartosik, Correlating elemental distribution with mechanical properties of TiN/SiN_x nanocomposite coatings, Scripta Mat. 170 (2019) 20–23, https://doi.org/10.1016/j.scriptamat.2019.05.020.
[16] R. Rachbauer, D. Holec, P.H. Mayrhofer, Increased thermal stability of Ti-Al-N thin films by Ta alloying, Surf. Coatings Technol. 211 (2012) 98–103, https://doi.org/10.1016/j.surfcoat.2011.07.009.
[17] R. Hollerweger, H. Riedl, J. Paulitsch, M. Arndt, R. Rachbauer, P. Polcik, S. Primig, P.H. Mayrhofer, Origin of high temperature oxidation resistance of Ti–Al–Ta–N coatings, Surf. Coatings Technol. 257 (2014) 78–86, https://doi.org/10.1016/j.surfcoat.2014.02.067.
[18] W.M. Seidl, M. Bartosik, S. Kolozsvári, H. Bolvardi, P.H. Mayrhofer, Influence of Ta on the fracture toughness of arc evaporated Ti-Al-N, Vacuum 150 (2018) 24–28, https://doi.org/10.1016/j.vacuum.2018.01.028.
[19] R. Hollerweger, H. Riedl, M. Arndt, S. Kolozsvari, S. Primig, P.H. Mayrhofer, Guide-lines for increasing the oxidation resistance of Ti-Al-N based coatings, Thin Solid Films 688 (2019) 137290 1–7, https://doi.org/10.1016/j.tsf.2019.05.009.
[20] N. Koutna, D. Holec, M. Friák, P.H. Mayrhofer, M. Šob, Stability and elasticity of meta-stable solid solutions and superlattices in the MoN-TaN system: first-principles calcula-tions, Mater. Des. 144 (2018) 310–322, https://doi.org/10.1016/j.matdes.2018.02.033.
[21] H. Asanuma, P. Polcik, S. Kolozsvari, F.F. Klimashin, H. Riedl, P.H. Mayrhofer, Cerium doping of Ti-Al-N coatings for excellent thermal stability and oxidation resistance, Surf. Coatings Technol. 326 (2017) 165–172, https://doi.org/10.1016/j.surfcoat.2017.07.037.
[22] A. Gil, B. Rajchel, N. Zheng, W.J. Quadakkers, H. Nickel, The influence of implanted chromium and yttrium on the oxidation behaviour of TiAl-based intermetallics, J. Mater. Sci. 30 (22) (1995) 5793–5798, https://doi.org/10.1007/BF00356723.

[23] B.A. Pint, Experimental observations in support of the dynamic segregation theory to explain the reactive element effect, Oxid. Met. 45 (1–2) (1996) 1–37, https://doi.org/10.1007/BF01046818.
[24] H.J. Grabke, M. Schütze (Eds.), Oxidation of Intermetallics, Wiley-VCH GmbH, Weinheim, 1998.
[25] E. Lang (Ed.), The role of Active Elements in the Oxidation Behaviour of High Temperature Metals and Alloys, Elsevier, London, 1989.
[26] D.P. Moon, Role of reactive elements in alloy protection, Mater. Sci. Technol. 5 (1989) 754–764, https://doi.org/10.1179/mst.1989.5.8.754.
[27] S. Mrowec, J. Jedliński, A. Gil, The influence of certain reactive elements on the oxidation behaviour of chromia- and alumina-forming alloys, Mater. Sci. Eng. A 120 (1989) 169–173, https://doi.org/10.1016/0921-5093(89)90735-1.
[28] L.A. Donohue, D.B. Lewis, M.M. Stack, S.B. Lyon, H.W. Wang, D. Rafaja, The influence of low concentrations of chromium and yttrium on the oxidation behaviour, residual stress and corrosion performance of TiAlN hard coatings on steel substrates, Vacuum 55 (2) (1999) 109–114, https://doi.org/10.1016/S0042-207X(99)00135-9.
[29] W.S. Choi, S.K. Hwang, C.M. Lee, Microstructure and chemical state of Ti1−xY 䍉NTi1−xYxN film deposited by reactive magnetron sputtering, J. Vac. Sci. Technol., A 18/6 (2000) 2914, https://doi.org/10.1116/1.1319680.
[30] M. Moser, P.H. Mayrhofer, Yttrium-induced structural changes in sputtered Ti1-xAlxN thin films, Scripta Mater 57 (4) (2007) 357–360, https://doi.org/10.1016/j.scriptamat.2007.04.019.
[31] H. Asanuma, F.F. Klimashin, P. Polcik, S. Kolozsvari, H. Riedl, P.H. Mayrhofer, Ther-momechanical properties and oxidation resistance of Ce–Si alloyed Ti–Al–N thin films, Vacuum 166 (2019) 231–238, https://doi.org/10.1016/j.vacuum.2019.05.016.
[32] H. Asanuma, F.F. Klimashin, P. Polcik, S. Kolozsvári, H. Riedl, P.H. Mayrhofer, Impact of lanthanum and boron on the growth, thermomechanical properties and oxidation resistance of Ti–Al–N thin films, Thin Solid Films 688 (2019) 137239 1–8, https://doi.org/10.1016/j.tsf.2019.04.014.
[33] H. Asanuma, F.F. Klimashin, P. Polcik, S. Kolozsvári, H. Riedl, P.H. Mayrhofer, Hard Ti–Al–N endowed with high heat-resistance through alloying with Ta and Ce, Surf. Coat. Technol. 372 (2019) 26–33, https://doi.org/10.1016/j.surfcoat.2019.05.018.
[34] P. Polcik, S. Kolozsvari, P.H. Mayrhofer, H. Riedl, Sputter target and method for producing a sputter target, WO 2018/158101 Al.
[35] W.C. Oliver, G.M. Pharr, An improved technique for determining hardness and elastic modulus using load and displacement sensing indentation experiments, J. Mater. Res. 7 (1992) 1564–1583, https://doi.org/10.1557/JMR.1992.1564.
[36] F.F. Klimashin, H. Riedl, D. Primetzhofer, J. Paulitsch, P.H. Mayrhofer, Composition driven phase evolution and mechanical properties of Mo–Cr–N hard coatings, J. Appl. Phys. 118 (2015), https://doi.org/10.1063/1.4926734 025305.
[37] A.C. Fischer-Cripps, Critical review of analysis and interpretation of nanoindentation test data, Surf. Coatings Technol. 200 (2006) 4153–4165, https://doi.org/10.1016/j.surfcoat.2005.03.018.
[38] F.F. Klimashin, P.H. Mayrhofer, Ab initio-guided development of super-hard Mo–Al–Cr–N coatings, Scr. Mater. 140 (2017) 27–30, https://doi.org/10.1016/j.scriptamat.2017.06.052.
[39] E.O. Hall, The deformation and ageing of mild steel: III discussion of results, Proc. Phys. Soc. Sect. B. 64 (1951) 747–753, https://doi.org/10.1088/0370-1301/64/9/303.
[40] N.J. Petch, The cleavage strength of polycrystals, J. Iron Steel Inst. 174 (1953) 25–28.
[41] C.S. Pande, K.P. Cooper, Nanomechanics of Hall-Petch relationship in nanocrystalline materials, Prog. Mater. Sci. 54 (2009) 689–706, https://doi.org/10.1016/j.pmatsci.2009.03.008.
[42] A. Leyland, A. Matthews, On the significance of the H/E ratio in wear control: a nanocomposite coating approach to optimised tribological behaviour, Wear 246 (2000) 1–11, https://doi.org/10.1016/S0043-1648(00)00488-9.
[43] X. Ding, X.T. Zeng, Y.C. Liu, Structure and properties of CrAlSiN Nanocomposite coatings deposited by lateral rotating cathod arc, Thin Solid Films 519 (2011) 1894–1900, https://doi.org/10.1016/J.TSF.2010.10.022.
[44] C.M. Koller, A. Kirnbauer, R. Rachbauer, S. Kolozsvári, P.H. Mayrhofer, Thermally-induced phase transformation sequence of arc evaporated Ta-Al-N coatings, Scr. Mater. 113 (2016) 75–78, https://doi.org/10.1016/j.scriptamat.2015.09.040.
[45] R. Rachbauer, S. Massl, E. Stergar, D. Holec, D. Kiener, J. Keckes, J. Patscheider, M. Stiefel, H. Leitner, P.H. Mayrhofer, Decomposition pathways in age hardening Ti-Al-N films, J. Appl. Phys. 110 (2011), https://doi.org/10.1063/1.3610451 023515.
[46] M. Hans, M. to Baben, D. Music, J. Ebenhöch, D. Primetzhofer, D. Kurapov, M. Arndt, H. Rudigier, J.M. Schneider, Effect of oxygen incorporation on the structure and elasticity of Ti-Al-O-N coatings synthesized by cathodic arc and high power pulsed magnetron sputtering, J. Appl. Phys. 116 (9) (2014) 2–7, https://doi.org/10.1063/1.4894776.
[47] F.F. Klimashin, L. Lobmaier, N. Koutná, D. Holec, P.H. Mayrhofer, The MoN–TaN system: Role of vacancies in phase stability and mechanical properties, Mater. Des. 202 (2021), https://doi.org/10.1016/j.matdes.2021.109568 109568.
[48] C.-S. Shin, D. Gall, N. Hellgren, J. Patscheider, I. Petrov, J.E. Greene, Vacancy hardening in single-crystal TiN_x(001) layers, JAP 93 (2003) 6025, https://doi.org/10.1063/1.1568521.
[49] S. Hofmann, H.A. Jehn, Selective oxidation and chemical state of Al and Ti in (Ti, Al)n coatings, Surf. Interface Anal. 12 (1988) 329–333, https://doi.org/10.1002/sia.740120602.
[50] F. Vaz, L. Rebouta, M. Andritschky, M.F. Da Silva, J.C. Soares, Thermal oxidation of $Ti_{1-x}Al_xN$ coatings in air, J. Eur. Ceram. Soc. 17 (1997) 1971–1977, https://doi.org/10.1016/S0955-2219(97)00050-2.
[51] G. Tammann, Über Anlauffarben von Metallen, Z. Anorg. Allg. Chem. 111 (1) (1920) 78–89, https://doi.org/10.1002/zaac.19201110107.
[52] G. Tammann, W. Köster, Metallographische Mitteilungen aus dem Institut für physikalische Chemie der Universität Göttingen. CV. Die Geschwindigkeit der Einwirkung von Sauerstoff, Schwefelwasserstoff und Halogenen auf Metalle, Zeitschrift für anorganische und allgemeine, Chemie 123 (1) (1922) 196–224, https://doi.org/10.1002/zaac.19221230115.
[53] C. Wagner, Beitrag zur Theorie des Anlaufvorgangs, Zeitschrift für physikalische Chemie 21B (1933) 25–41, https://doi.org/10.1515/zpch-1933-2105.
[54] A. Fick, Ueber diffusion, Ann. Phys. 94 (1855) 59–86, https://doi.org/10.1002/andp.18551700105.
[55] A. Atkinson, Transport processes during the growth of oxide films at elevated temperature, Rev. Mod. Phys. 57 (2) (1985) 437–470, https://doi.org/10.1103/RevModPhys.57.437.
[56] N. Cabrera, N.F. Mott, Theory of the oxidation of metal, Rep. Prog. Phys. 12 (1949) 163–184, https://doi.org/10.1088/0034-4885/12/1/308.
[57] W.J. Shen, M.H. Tsai, K.Y. Tsai, C.C. Juan, C.W. Tsai, J.W. Yeh, Y.S. Chang, Superior oxidation resistance of (Al0.34Cr0.22Nb0.11Si0.11Ti0.22)50N50 highentropy nitride, J. Electrochem. Soc. 160 (11) (2013) 531–535, https://doi.org/10.1149/2.028311jes.
[58] W.J. Quadakkers, D. Naumenko, E. Wessel, V. Kochubey, L. Singheiser, Growth rates of alumina scales on Fe–Cr–Al alloys, Oxid. Met. 61 (2004) 17–37, https://doi.org/10.1023/B:OXID.0000016274.78642.